Periodica Polytechnica Civil Engineering, 68(3), pp. 946–960, 2024

Prediction of Rock's Brittleness and Dynamic Properties Utilizing Effective Artificial Intelligence Approaches

Yonggang Xie[1,2], Lili Wang[1,2], Yonghong Gu[1,2], Xiangdong Gu[3], Shijun Chen[4*], Mohammad Khajehzadeh[5], Saeedeh Hosseini[6]

[1] Oil and Gas Technology Institute, PetroChina Changqing Oilfield Company, Xi 'an 710018, Shaanxi, China
[2] National Engineering Laboratory of low-permeability Oil & Gas Exploration and Development, Xi 'an 710018, Shaanxi, China
[3] Natural Gas Evaluation Project, Department of Changqing oil field, Qingyang 74500, Gansu Province, P.R. China
[4] School of Chemistry and Chemical Engineering, Xi'an Shiyou University, 710065, Shaanxi Province, P.R. China
[5] Department of Civil Engineering, Anar Branch, Islamic Azad University, Anar 7741943615, Iran
[6] Department of Geology, Payame Noor University, Tehran PC 19395-3697, Iran
[*] Corresponding author, e-mail: csjun@xsyu.edu.cn

Received: 08 August 2023, Accepted: 27 March 2024, Published online: 16 May 2024

Abstract

This research aims to determine the brittleness index (BI) and engineering properties of limestone specimens. In addition, this study evaluates the effect of moisture on the developed models to predict the BI and shear wave velocity (*Vs*), based on the point load index (Is50), dry and saturated tensile strength (*Ts-d* and *Ts-s*), and porosity. Gaussian process regression (GPR), multilayer feed-forward neural network (MFFNN), and multiple linear regression (MLR) predictive models were utilized. Microscopic examination of the limestone specimens revealed that calcite is the predominant mineral. It was observed that samples with higher calcite content exhibited greater brittleness and strength properties while having lower porosity. The results obtained from the MLR analysis demonstrated that it is possible to accurately forecast the brittleness index (BI), as well as the dry and saturated shear wave velocities (*Vs-d* and *Vs-s*) at the specific sites under investigation. The moisture effect on developed models showed that *Vs* prediction in dry conditions (*Vs-d*) was less accurate compared to the saturated conditions (*Vs-s*). Conversely, the relationships developed for estimating the BI in dry conditions exhibited higher accuracy. The analysis of all model assumptions using MLR indicated that the models could be reliably utilized. However, the MFFNN and GPR methods were found to be more conservative in estimating these properties. Moreover, the study identified the best transfer function and training algorithm for predicting *Vs* and BI. The evaluation metrics, such as R^2 and RMSE revealed that GPR demonstrated higher precision compared to MFFNN and MLR.

Keywords

engineering properties, brittleness, dry and saturated conditions, GPR, MFFNN, MLR

1 Introduction

The brittleness and engineering properties of rock foundations are crucial factors in various engineering applications, including the design of dams and tunnels, rock blasting, investigation of rock slope stability, and underground drilling. Meeting these geotechnical requirements necessitates the determination of these characteristics. However, obtaining samples with the appropriate geometry and quality from jointed rocks is a challenging task, making it difficult to prepare suitable samples. Therefore, prediction models have been developed based on physical characteristics and wave velocity [1, 2]. Numerous studies have been performed by various researchers to estimate the geo-mechanical properties in dry and saturated conditions [3–5].

Brittleness is a function of strength that indicates rock strength against deformation in the elastic range. There is no standardized concept and method for measuring brittleness [6]. Brittleness is usually obtained from the uniaxial compressive strength (UCS) to tensile strength (*Ts*) ratio [7, 8]. Performing uniaxial compressive strength test requires a lot of money and time, which is not cost-effective for small projects [2]. Punch test results and index tests such

Cite this article as: Xie, Y., Wang, L., Gu, Y., Gu, X., Chen, S., Khajehzadeh, M., Hosseini, S. "Prediction of Rock's Brittleness and Dynamic Properties Utilizing Effective Artificial Intelligence Approaches", Periodica Polytechnica Civil Engineering, 68(3), pp. 946–960, 2024. https://doi.org/10.3311/PPci.23156

as Is50 and porosity are usually used to estimate the brittleness [7, 9]. Yagiz et al. [10] estimated BI using soft computing methods. On the other hand, shear wave velocity provides valuable information about the properties of carbonate rocks, especially in the identification of oil reservoirs.

Several scholars used MFFNN and MLR methods to predict the brittleness index using nondestructive tests and physical characteristics [11–13]. Altindag and Guney [14] presented some relationships to estimate brittleness based on UCS, Schmidt hardness number, and *Ts*. Akbar and Musu [15] studied the effect of mineralogy on the brittleness. Studies have revealed that MFFNN has high precision to estimate the *Vs* rock samples [16, 17]. Singh and Kanli (2016) [18] using MFFNN estimated the *Vs* of the carbonate rocks. Alizadeh et al. [19] proposed some models using MFFNN and MLR to estimate the dynamic properties of the sandstone rocks. Mehrad et al. [20] predicted the *Vs* of the carbonate rocks using artificial intelligence techniques. Also, Al-Dousari et al. [21] developed several empirical relationships to estimate the Vs of sedimentary rocks. Zheng et al. [22] used GPR, MFFNN, and MLR to predict tensile strength. Also, Gao et al. [23] estimated rock fragmentation using the GPR method. In a study conducted by Fang et al. [24], the authors employed MFFNN and GPR techniques to estimate the tensile strength of rock samples. Jahed Armaghani et al. [25] focused on predicting the BI using the SVM method. Viswanathan and Samui [26] utilized the GPR method to predict rock depth in their study. Mahmoodzadeh et al. [27] predicted rock quality designation (RQD) using several methods and found that the GPR method outperformed other methods. In a study conducted by Lawal et al. [28], GPR, artificial neural network (ANN), and response surface method (RSM) were used to predict static and dynamic rock properties based on *P*-wave and rock density. The results of their study demonstrated that GPR yielded more accurate results compared to ANN and RSM models. Lee and Lumley [29] proposed some relationships between input features and brittleness. Li et al. [30] evaluated the rock brittleness index under dynamic load. They employed experimental techniques and machine learning algorithms to develop a predictive model for assessing rock brittleness under varying loading conditions. Fang et al. [31] presented a brittleness index prediction method for tight reservoirs based on grey correlation and analytic hierarchical process. Their approach integrated multiple parameters and showed promise in predicting brittleness in challenging reservoirs.

In this study, after determining geomechanical properties in dry and saturated conditions on the limestone specimens of the Asmari formation (AF) in Khersan II and Bazoft dam sites, the results were presented and models were analyzed using GPR, MFFNN, and MLR to estimate *Vs*, and BI. Finally, the moisture effect on these models was assessed.

2 Case studies

The proposed Khersan-II dam site is located in Lordegan city, within the Chahar-Mahal and Bakhtiari province in western Iran (Fig. 1). The dam is planned to have a height of 240 meters and a reservoir volume of 2142 million cubic meters. The site is situated on the Khersan River, in the southwestern region of Iran, specifically within the Zagros highlands. The abutments of the site are formed by the Asmari and Gachsaran formations, as shown in Fig. 1. For the analyses conducted, a total of 56 samples were collected from the abutment foundations (AF) of the Khersan-II dam site.

The Bazoft dam, currently in the design stage, is planned to be a double-arched concrete dam with a height of 211 meters. The dam site is characterized by the presence of the Jahrom formation, which serves as the right abutment, the riverbed, and the lower section of the left support. Additionally, the abutment foundations (AF) constitute the middle and upper section of the left support, as illustrated in Fig. 1. For analytical purposes, a total of 10 samples were collected from the abutments of the Bazoft dam site.

3 Materials and methods

3.1 Laboratory tests

Experiments were implemented on the 68 dry and saturated specimens without cracks obtained from the limestones of the AF. Joints and discontinuities cause heterogeneity and asymmetric stress concentration on the specimens during loading. This causes errors in the measured mechanical properties [2]. The samples were prepared according to the ISRM standard with a diameter of 54 mm [32]. Physical experiments such as porosity (*n*) and water absorption (*Wa*) by weight were done based on the ISRM suggested methods [32]. After smoothing two ends of specimens with grease, the *Vp* and *Vs* were measured on samples using the ASTM standard with a frequency of 0.5 MHz [33]. Uniaxial compressive strength (UCS) experiments were performed on the specimens with a loading rate of 0.8 MPa/s based on the ISRM [32].

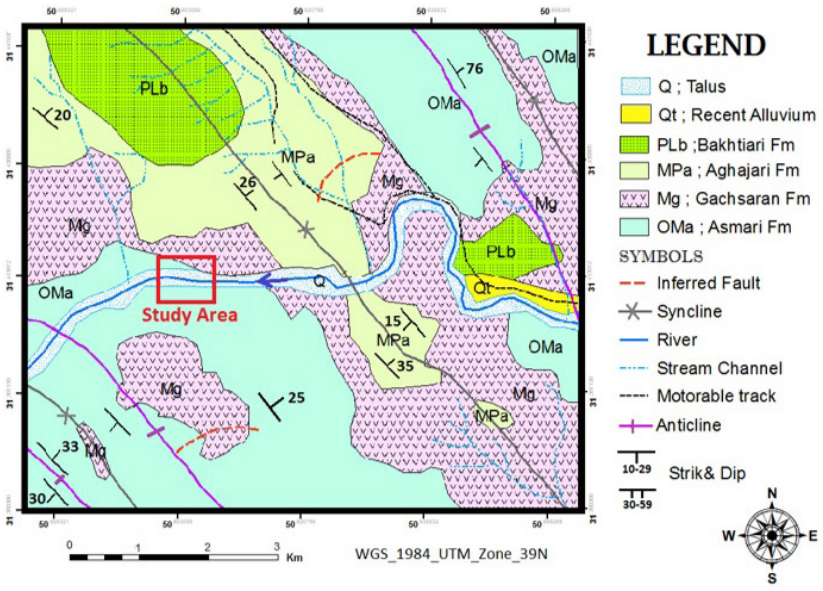

(a)

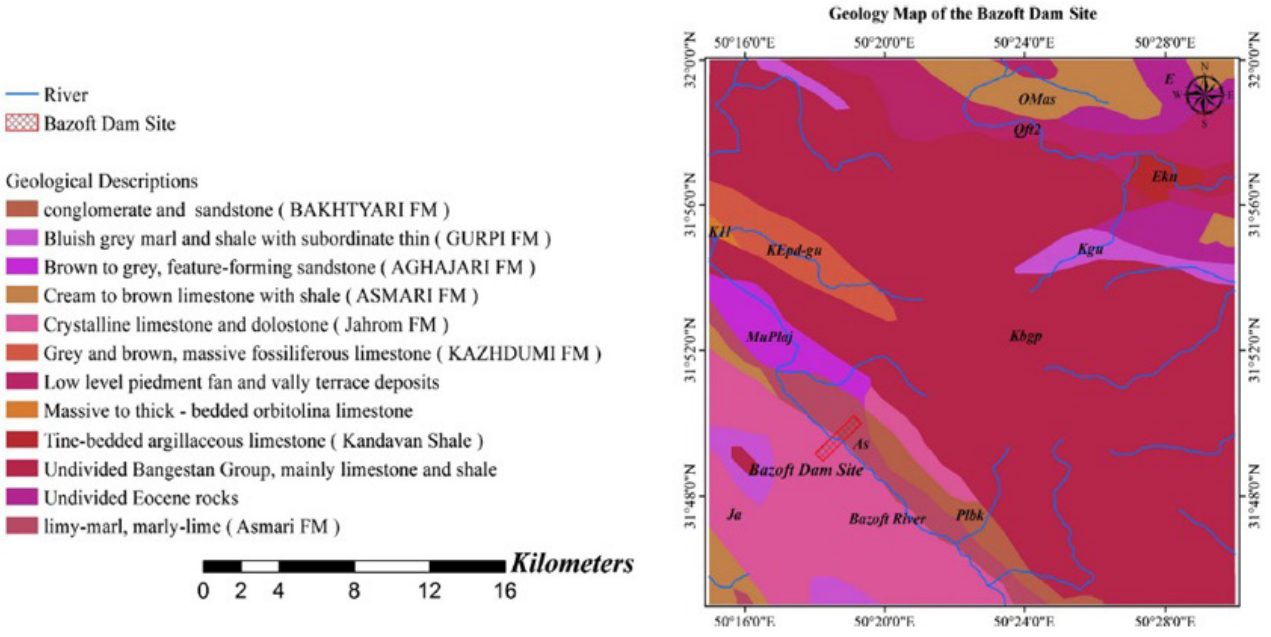

(b)

Fig. 1 Geological map of (a) Khersan-II and (b) Bazoft dam sites

Then, the stress-strain curves were drawn for determining UCS and static elastic modulus (*Es*). Using the slope of the tangent line on the point of 50% of the ultimate strength, the *Es* was measured. Brazilian tensile strength test was performed on the dry and saturated cores [34]. In the Brazilian test, the diameter of the samples was 54 mm with a thickness-to-diameter ratio of one. The point load index (Is50) tests were conducted on the cylindrical and irregular samples, then using the proposed methods the Is50 was computed [35].

Also, the brittleness index was measured using a punch penetration test. This is a very expensive method which determines the exact amount of rock brittleness. In this experiment, a cone-shaped penetrator presses against the rock by the force applied by the jack, and the amount of force and displacement of the penetrator is measured and stored in a computer. In this test, the sample is molded into a steel cylindrical mold by a plaster. Then, the brittleness is calculated from Eq. (1) using the force-displacement diagram [36].

$$\mathrm{BI} = \frac{F_{\max}}{P_{\max}} \tag{1}$$

In Eq. (1), BI is the brittleness index (kN/mm), $F_{\max}$ is the maximum force (kN) and $P_{\max}$ is the maximum penetration (mm).

3.2 Gaussian process regression (GPR)

A Gaussian process (GP) is a collection of random variables that are characterized by following a Gaussian distribution. The GPR is a method used to classify data by leveraging the underlying structures present within it. In a Gaussian process, there is a distribution function referred to as f which is defined as a mapping from the input space $\boldsymbol{X}$ to the real space R. For any finite subset of X, the marginal distribution of $f(x_1), f(x_2), \ldots, f(x_n)$ conforms to a multivariate normal distribution, as discussed in Lawal et al. [28]. The parametric Gaussian process is defined as follows using $m(x)$ mean function and $k(x_i, x_j)$ covariance function.

$$f \left| X \sim N\left(m(x), \quad \boldsymbol{K}\left(\boldsymbol{X}, \boldsymbol{X}\right)\right)\right| \tag{2}$$

An equivalent form of Eq. (2) is:

$$f(x) \sim \mathrm{GP}\left(m(x), \quad k\left(x_i, x_j\right)\right). \tag{3}$$

In the above relationship, the $\boldsymbol{X}$ matrix rows are input vectors, f is a vector of function values, and $\boldsymbol{K}(\boldsymbol{X}, \boldsymbol{X})$ represents the $n \times n$ covariance matrix so that $K_{ij} = k(x_i, x_j)$.

In order to initialize the GP, the regression model of the Gaussian process, considering y as an observation along with the Gaussian error ε, is expressed as Eq. (4), [28]:

$$y = f(x) + \varepsilon, \ \ \varepsilon \sim N\left(0, \sigma_n^2\right). \tag{4}$$

The common distribution of y training outputs and f_* test outputs with zero average function is (Eq. (5)):

$$\begin{bmatrix} y \\ f_* \end{bmatrix} \sim N\left(0, \begin{bmatrix} \boldsymbol{K}\left(\boldsymbol{X}, \boldsymbol{X}\right) + \sigma_n^2 I & \boldsymbol{K}\left(\boldsymbol{X}, \boldsymbol{X}_*\right) \\ \boldsymbol{K}\left(\boldsymbol{X}_*, \boldsymbol{X}\right) & \boldsymbol{K}\left(\boldsymbol{X}_*, \boldsymbol{X}_*\right) \end{bmatrix}\right). \tag{5}$$

Where X_* and $\boldsymbol{X}$ are the test and training data matrix of the model, respectively. By binding f_* on the y observation, the prediction of the distribution can be displayed as follows (Eq. (6)):

$$f_* \left| X, y, X_* \sim N\left(\bar{f}_*, V\left(f_*\right)\right)\right|. \tag{6}$$

Where $\bar{f}_*$ and $V(f_*)$ are obtained from Eq. (7) and Eq. (8).

$$\bar{f}_* = \boldsymbol{K}\left(\boldsymbol{X}_*, \boldsymbol{X}\right)\left[\boldsymbol{K}\left(\boldsymbol{X}, \boldsymbol{X}\right) + \sigma_n^2 I\right]^{-1} y \tag{7}$$

$$V\left(f_*\right) = \boldsymbol{K}\left(\boldsymbol{X}_*, \boldsymbol{X}_*\right) - \boldsymbol{K}\left(\boldsymbol{X}_*, \boldsymbol{X}\right)\left[\boldsymbol{K}\left(\boldsymbol{X}, \boldsymbol{X}\right) + \sigma_n^2 I\right]^{-1} \cdot \boldsymbol{K}\left(\boldsymbol{X}, \boldsymbol{X}_*\right) \tag{8}$$

For the covariance matrices, the symbols $\boldsymbol{K}(\boldsymbol{X}_*, \boldsymbol{X}_*)$, $\boldsymbol{K}(\boldsymbol{X}, \boldsymbol{X}_*)$, and $\boldsymbol{K}(\boldsymbol{X}_*, \boldsymbol{X})$ are like to the former $\boldsymbol{K}(\boldsymbol{X}, \boldsymbol{X})$ symbol. Based on Eq. (6), the forecast mean is calculated by combining the observed values of y using a linear approach. The coding of GPR relies on the assumption that inputs that are in close proximity are likely to yield similar outputs. As a result, higher weights are assigned to samples with similar values.

3.3 Multilayer feed-forward neural network (MFFNN)

MFFNN is a fundamental and widely used architecture in the field of artificial neural networks (ANNs). It's composed of multiple layers of interconnected neurons, where information flows strictly in one direction, from the input layer through one or more hidden layers to the output layer. Each neuron in a layer is connected to every neuron in the subsequent layer, and each connection is associated with a weight. Key components and characteristics of the MFFNN have been widely discussed in previous researches [2, 11–13, 16, 17].

Finally, the accuracy of the used methods and equations was appraised by computing the R^2, RMSE and variance account factor (VAF).

4 Results

4.1 Laboratory results

Studies on 68 samples of the thin sections showed that samples contain microfossils of *Echinoid*, *Pelecypoda* and *Foraminifera* (Fig. 2). Based on the Dunham [37] textural classification, the specimens are classified as Wackestone, Packstone and Grainstone. The fossils showed that AF has been deposited in a swamp environment. Fig. 2 displays some thin sections of AF formation.

The X-ray fluorescence (XRF) using Philips PW1480 model, the percentage of main oxides of the samples was determined. The XRF results on 10 samples are presented in Table 1. It is observed that the main oxide of the specimens is the CaO.

Results of physical and mechanical experiments on specimens are displayed in Table 2. Normality tests according to the skewness and kurtosis tests (Table 2), the Kolmograph Smirnov and Shapiro Wilk tests showed that the variables are normal at the 5% error level. The BI is in the range of 5.79 kN/mm to 25.11 kN/mm with an average of 18.73 kN/mm. This index, according to the

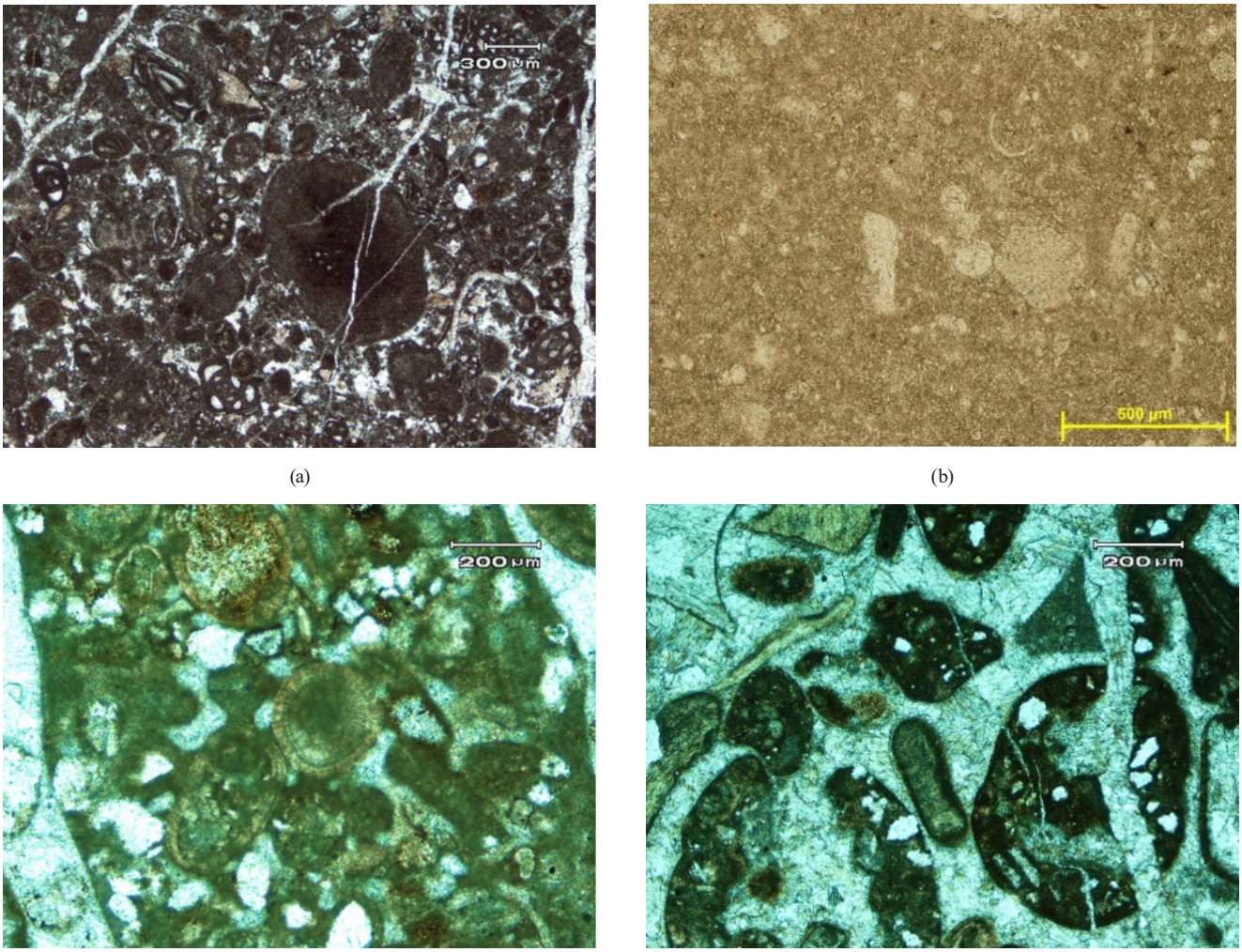

(a) (b)

(c)

Fig. 2 The images of thin sections: (a) Wackestone to Packstone containing Ploid and Interclast, (b) Wackestone containing *Foraminifera*, *Echinoid* and *Placypoda*, (c) Grainstone with Algal Foraminifer

Table 1 The XRF results on 10 samples

Components (%)	Samples									
	1	2	3	4	5	6	7	8	9	10
SiO_2	2.12	2.43	2	2.3	3.98	3.5	0.8	2.1	2.3	2.06
Fe_2O_3	0.41	0.28	0.28	0.25	0.3	0.15	0.12	0.3	0.5	1
Al_2O_3	2.68	2.70	0.68	2.2	0.9	1.2	0.15	0.72	0.2	1
CaO	64.56	60.12	61	65.21	50.9	51.1	55.2	53.1	53	56.9
MgO	0.75	0.24	20.3	0.3	18.7	2	0.3	0.22	0.2	18.2
K_2O	0.2	0.41	0.17	0.18	0.21	0.18	0.25	0.12	0.11	0.3
P_2O_3	0.05	0.04	0.06	0.07	0.02	0.04	0.07	0.05	0.07	0.09
SO_3	0.07	0.01	0.07	0.05	0.12	0.21	0.05	0.02	0.14	0.2
TiO_2	1	2.1	0.08	0.1	0.04	0.05	0.02	0.03	0.07	0.05
SrO	0.15	0.56	0.12	0.11	0.01	0.02	0.21	0.12	0.11	0.01
L.O.I.	29.17	32.16	15.25	29.44	24.82	41.65	42.83	43.22	43.3	20.19

classifications of Yagiz [36] and AFTES [38] was classified in the non-brittle and brittle classes, respectively. The *Vs* varies from 1.07 to 3.36 km/s (Table 2). Also, the mean of dry and saturated UCS are 45.75 MPa and 38.17 MPa, respectively. The average porosity (*n*) and dry point load index (Is50) are also 5.73% and 4.25 MPa,

Table 2 The measured values on each sample

Sample	UCS (MPa) dry	*Es*-dry (GPa)	*n*	*Tsd* (MPa)	Is50-dry (MPa)	*Tss* (MPa)	*Vs*-sat. (km/s)	*Vs*-dry (km/s)	*Vp* (km/s) dry	*Vp* (km/s) sat	BI (kN/mm)	Dry density (g/cm^3)	*Ed*-dry (GPa)
S1	64.63	17.14	2.00	7.19	6.15	6.93	3.19	3.12	5.537	5.623	24.00	2.47	61.01
S2	59.42	23.41	3.00	6.61	5.44	6.38	3.07	3.00	5.273	5.391	23.53	2.45	55.49
S3	60.89	12.95	3.00	6.77	5.64	6.53	3.11	2.60	5.347	5.457	23.91	2.45	44.72
S4	41.30	7.80	7.00	4.59	2.95	4.43	2.64	2.56	4.355	4.584	18.95	2.30	37.24
S5	69.72	15.77	1.25	7.76	6.85	7.48	3.31	2.25	5.795	5.850	22.00	2.41	34.35
S6	40.28	12.08	7.00	4.48	2.82	4.32	2.62	2.54	4.304	4.538	18.69	2.36	37.44
S7	56.70	18.05	3.60	6.31	5.06	6.08	3.01	2.93	5.135	5.270	22.85	2.44	52.87
S8	68.14	16.00	5.00	7.58	6.63	7.31	3.28	2.58	5.714	5.780	23.00	2.41	44.16
S9	65.65	18.21	2.00	7.30	6.29	7.04	3.22	3.15	5.588	5.669	25.11	2.45	61.45
S10	49.34	8.84	5.00	5.49	4.06	5.29	2.83	2.75	4.762	4.942	20.98	2.31	43.82
S11	64.18	14.31	2.00	7.14	6.09	6.89	3.18	2.71	5.514	5.603	24.74	2.39	47.11
S12	50.70	21.33	5.00	5.64	4.24	5.44	2.87	2.79	4.831	5.002	21.33	2.49	48.40
S13	55.57	19.85	4.00	6.18	4.91	5.96	2.98	2.91	5.078	5.219	22.56	2.47	52.38
S14	57.27	15.00	4.00	6.37	5.14	6.14	3.02	2.95	5.164	5.295	22.99	2.20	48.07
S15	52.74	13.98	5.00	5.87	4.52	5.66	2.91	2.84	4.934	5.093	21.84	2.39	48.11
S16	48.66	27.51	5.00	5.41	3.96	5.22	2.82	2.74	4.728	4.912	20.81	2.58	48.25
S17	49.45	14.00	5.00	5.50	4.07	5.31	2.84	2.58	4.768	4.947	21.01	2.39	40.96
S18	45.93	16.91	6.00	5.11	3.59	4.93	2.75	2.67	4.590	4.790	20.12	2.43	43.12
S19	51.95	31.22	5.00	5.78	4.41	5.57	2.89	2.82	4.894	5.058	21.64	2.63	52.33
S20	65.42	11.87	2.00	7.28	6.26	7.02	3.21	3.14	4.577	5.659	20.05	2.36	49.03
S21	64.52	31.22	2.00	7.18	6.14	6.92	3.19	3.12	5.531	5.618	24.82	2.63	64.92
S22	39.72	31.22	4.00	4.42	2.74	4.26	2.61	2.52	4.275	4.513	18.54	2.63	41.30
S23	59.19	24.90	3.00	6.58	5.41	6.35	3.07	2.99	5.261	5.381	23.48	2.54	57.39
S24	57.16	18.63	3.00	6.36	5.13	6.13	3.02	2.94	5.158	5.290	22.96	2.45	53.47
S25	39.72	20.05	6.00	4.42	4.00	4.26	2.61	2.52	4.275	4.513	18.54	2.47	38.79
S26	46.17	18.63	5.00	5.14	3.62	4.95	2.76	2.68	4.602	4.801	20.18	2.45	43.76
S27	62.37	40.00	3.00	6.94	5.84	6.69	3.14	3.07	5.422	5.522	24.28	2.76	65.66
S28	60.44	27.84	3.00	6.72	5.58	6.48	3.09	3.02	5.324	5.436	23.79	2.58	59.58
S29	52.74	35.91	5.00	5.87	4.52	5.66	2.91	2.84	4.934	5.093	21.84	2.70	54.43
S30	15.43	9.40	12.11	1.72	2.00	1.66	1.93	1.83	2.821	3.233	16.00	2.32	17.66
S31	18.45	11.61	11.51	2.05	3.00	1.98	2.01	1.91	2.990	3.382	17.00	2.35	19.83
S32	18.45	11.61	11.51	2.05	3.00	1.98	2.01	1.91	2.990	3.382	16.00	2.35	19.83
S33	12.41	7.44	12.72	1.38	1.98	1.33	1.85	1.75	2.652	3.085	10.43	2.29	15.64
S34	10.84	2.38	14.83	1.21	0.40	1.16	1.58	1.47	2.061	2.565	10.00	2.22	9.43
S35	22.15	6.55	10.77	2.46	2.20	2.38	1.81	1.71	2.568	3.010	16.00	2.28	14.68
S36	14.12	3.57	12.38	1.57	2.00	1.52	1.66	1.55	2.230	2.713	15.00	2.24	11.10
S37	8.90	2.00	14.85	0.99	0.30	0.95	1.19	1.07	1.720	1.822	11.00	2.21	5.98
S38	6.04	2.00	13.99	0.67	0.50	0.65	1.42	1.31	1.724	2.268	7.00	2.21	6.22
S39	10.94	2.38	13.01	1.22	0.20	1.17	1.58	1.47	2.061	2.565	7.48	2.22	9.43
S40	27.07	8.39	9.79	3.01	1.01	2.90	1.89	1.79	2.736	3.159	12.00	2.31	16.64
S41	38.97	12.82	7.41	4.33	2.64	4.18	2.05	1.95	3.074	3.456	12.54	2.37	20.97
S42	10.94	2.38	13.01	1.22	1.00	1.17	1.58	1.47	2.061	2.565	7.48	2.22	9.43
S43	41.83	13.88	6.83	4.65	3.03	4.49	2.25	2.15	3.496	3.827	14.65	2.38	26.38
S44	67.14	23.30	1.77	7.47	4.00	7.20	2.59	2.55	4.340	4.570	18.87	2.52	40.58

Table 2 The measured values on each sample (continued)

Sample	UCS (MPa) dry	*Es*-dry (GPa)	*n*	*Tsd* (MPa)	Is50-dry (MPa)	*Tss* (MPa)	*Vs*-sat. (km/s)	*Vs*-dry (km/s)	*Vp* (km/s) dry	*Vp* (km/s) sat	BI (kN/mm)	Dry density (g/cm^3)	*Ed*-dry (GPa)
S45	38.25	15.33	1.81	4.25	2.54	4.10	2.74	2.15	3.496	3.827	14.65	2.40	26.61
S46	50.73	17.19	5.00	5.64	4.25	5.44	2.81	2.55	4.340	4.570	18.87	2.43	39.17
S47	50.73	17.19	2.90	5.64	4.25	5.44	2.85	2.55	4.420	4.570	19.27	2.43	39.62
S48	67.14	23.30	5.07	7.47	5.50	7.20	3.20	2.55	4.340	4.570	18.87	2.52	40.58
S49	50.73	17.19	9.96	5.64	4.25	5.44	2.78	2.55	4.340	4.570	18.87	2.43	39.17
S50	64.29	22.24	2.00	7.15	6.10	6.90	2.64	2.55	4.340	4.570	18.87	2.50	40.33
S51	50.73	17.19	5.73	5.64	4.25	5.44	3.22	2.55	4.340	4.570	18.87	2.43	39.17
S52	63.57	21.97	2.39	7.07	6.01	6.82	2.64	2.55	4.340	4.570	18.87	2.50	40.27
S53	64.29	22.24	0.36	7.15	6.10	6.90	3.21	2.55	4.340	4.570	18.87	2.50	40.33
S54	50.73	17.19	5.19	5.64	4.25	5.44	2.71	2.55	4.340	4.570	18.87	2.43	39.17
S55	40.71	13.47	7.06	4.53	4.00	4.37	2.34	2.71	5.000	6.056	20.00	2.38	45.01
S56	62.86	21.71	2.00	6.99	5.91	6.74	2.66	1.95	5.252	3.085	18.00	2.60	28.08
S57	65.00	16.55	4.20	7.23	6.30	6.97	2.61	2.54	4.500	4.650	18.00	2.42	39.57
S58	51.73	16.04	4.50	5.75	4.85	5.55	2.61	2.51	4.450	4.570	18.00	2.41	38.54
S59	65.20	16.50	4.60	7.25	7.20	7.00	2.62	2.50	4.680	4.980	18.00	2.42	39.36
S60	45.00	17.02	4.80	5.01	7.30	4.83	2.63	2.53	5.600	6.540	18.00	2.43	42.65
S61	51.2	16.325	4.70	5.70	4.56	5.49	2.63	2.51	4.7	4.98	18.00	2.42	39.64
S62	42	14.812	4.65	4.67	3.6	4.51	2.64	2.51	3.9	4.1	18.00	2.40	34.63
S63	72	17.228	4.89	8.01	5.6	7.73	2.62	2.54	4.98	5.3	18.00	2.43	41.55
S64	63	17.572	5.1	7.01	6.3	6.76	2.64	2.53	6	6.1	18.00	2.44	43.42
S65	60.44	17.259	5	6.72	5.51	6.48	2.64	2.56	5.1	5.26	18.00	2.43	42.45
S66	54	17.279	4	6.01	5.5	5.79	2.63	2.56	5.3	5.2	18.00	2.43	42.97
Min.	10.84	2.00	0.36	0.67	0.20	0.66	1.19	1.07	1.72	1.82	7.00	2.20	5.98
Max.	72.00	40.00	14.85	8.01	7.30	7.89	3.31	3.15	6.00	6.54	25.11	2.76	65.66
Mean	47.56	16.62	5.73	5.31	4.29	5.23	2.63	2.46	4.35	4.58	18.68	2.42	38.42

Symbols: UCS: Uniaxial compressive strength, *Es*: static elastic modulus, *Ed*: dynamic elastic modulus, *Tsd*: dry tensile strength, *Tss*: saturated tensile strength, Is50: point load value, *Vs*: shear wave velocity, *Vp*: compressional wave velocity, BI: brittleness index

respectively. The strength features of the Bazoft dam site are greater than the specimens of Khersan-II dam site. Microscopic studies of the samples showed that samples were classified from the Wackestone (mostly samples from Khersan-II dam site) to the Grainstone (mostly samples from Khersan-II dam site). Also based on XRF results (Table 1) and rock mechanic test results the samples with high calcite mineral showed high brittleness and strength properties and low porosity. Mineralogy and physical properties control geo-mechanical characteristics of the carbonates [22]. It is observed that the saturation of the samples has reduced the strength properties and increased the wave velocity (Table 2). The values of UCS and *Es* in the saturated state are less than the values of these parameters in the dry state. Decreased compressive strength at a saturated state has been also reported by other scholars [39, 40]. High-porosity rocks, when saturated, can show a large range of wave velocities [2, 41]. Vásárhelyi [41] stated that UCS in the saturated state is about 75.6% of the UCS in the dry state.

4.2 Simple regression (SR)

In this section, the relationships between independent and dependent variables by simple regression method were investigated and the relationships that showed a coefficient of determination greater than 0.50 were evaluated in more detail based on RMSE and VAF criteria (results in Table 3). In Fig. 3, the influence of various factors on the brittleness index is presented. These factors include dry Brazilian tensile strength (*Ts*-dry), saturated Brazilian tensile strength (*Ts*-sat.), dry point load index (Is-dry), total porosity (*n*), dry shear wave velocity (*Vs*-dry), saturated shear wave velocity (*Vs*-sat.), dry compressional wave velocity (*Vp*-dry), and saturated compressional wave

Table 3 Empirical relations to estimate BI and *Vs* of the limstone rocks

Equations	R^2	RMSE	%VAF
BI = 3.52 $Vp_{(sat.)}$ + 2.64	0.72	3.12	71.02
BI = 3.32 $Vp_{(d)}$ + 4.41	0.77	3.09	76.95
BI = 1.00 $Ts_{(d)}$ + 11.02	0.71	3.01	70.21
BI = −0.92n + 24.042	0.62	3.49	61.80
BI = 1.88 Is50 + 10.70	0.60	3.85	59.65
BI = 8.44 $Es_{(d)}^{0.2984}$	0.62	4.06	60.98
$Vs_{(d)}$ = −0.12n + 3.17	0.67	3.85	66.65
$Vs_{(sat.)}$ = −0.124n + 3.34	0.79	2.00	77.98
$Vs_{(d)}$ = 0.47 $Vp_{(sat.)}$ + 0.34	0.88	1.29	87.32
$Vs_{(s)}$ = 0.40 $Vp_{(d)}$ + 0.90	0.80	1.98	79.35
$Vs_{(d)}$ = 0.941 $Vs_{(sat.)}$ + 0.02	0.86	1.38	85.64
$Vs_{(d)}$ = 0.44 $Vp_{(d)}$ + 0.61	0.92	1.11	91.89
$Vs_{(d)}$ = 1.70 $(Is50)^{0.28}$	0.72	1.78	71.98
$Vs_{(s)}$ = 1.82 $Is50^{(0.27)}$	0.76	1.98	75.76
$Vs_{(s)}$ = 0.12 $Ts_{(d)}$ + 1.74	0.67	3.25	66.35
$Vs_{(d)}$ = 0.12 $Ts_{(d)}$ + 1.56	0.73	2.29	72.42

velocity (*Vp*-sat.). The graph demonstrates how these parameters affect the brittleness index. According to the Taylor [42] criterion, a coefficient of determination (R^2) greater than 50% is considered as a strong correlation. From Fig. 3, it is evident that the parameter with the most significant impact on the brittleness index of limestone rocks is the dry shear wave velocity (*Vs*) condition. On the other hand, the parameter with the least effect on the brittleness index is the tensile strength under saturated conditions. The relationships between brittleness and static properties (UCS and *Es*) show the fitted correlations are moderate and the compressive strength under saturation conditions has the least effect on this index (Fig. 3).

Fig. 4 shows the relationships among properties in dry and saturated conditions. It is observed that the greatest effect on *Vs* is related to the *Vp* in dry conditions (Fig. 4). The correction factor, represented by the ratio *Ed*/*Es*, is a well-established metric, averaging at 2.53 for dry samples as evidenced in this study's findings. Discrepancies observed between dynamic and static properties can be ascribed to factors including cementation, porosity, amplitude, frequency, and pore water pressure. Moreover, variations in stress and strain levels across different measurement techniques significantly contribute to the observed differences [16].

According to Table 3, wave velocities have the greatest impact on the brittleness of limestone rocks. Modulus of elasticity also has a moderate effect on brittleness. Compressional wave velocity also shows the greatest influence on *Vs*. Various studies have reported that the *Vp* has a great effect on shear wave velocity [2, 19].

4.3 The MLR to estimate *Vs* and brittleness index

In the current study, six models by MLR method were developed for forecasting *Vs-d*, *Vs-s*, and BI using porosity, dry Is50, and dry and saturated tensile strength (*Ts-d* and *Ts-s*) on 66 samples of the limestone of the studied sites. The *Vs-d*, *Vs-s*, and BI relationships based on the independent variables and according to Table 4 are in the form of Eqs. (9)–(14). To display the correlation among the variables in 3 dimensions using MATLAB software [43], the curve fitting command was used. In this method, some of the best relationships between dependent and independent parameters used in relationships 9 to 14 are shown in Fig. 5. Based on Fig. 5, the lower the porosity of the samples and the higher the point load index, the greater the brittleness index.

$$\mathrm{BI} = -0.722n + 0.46Ts_{(d)} - 0.161\mathrm{Is50} + 19.918 \tag{9}$$

$$\mathrm{BI} = -0.653n + 0.041Ts_{(s)} + 0.546\mathrm{Is50} + 19.717 \tag{10}$$

$$Vs_{(d)} = -0.084n + 0.003Ts_{(s)} + 0.063\mathrm{Is50} + 2.682 \tag{11}$$

$$Vs_{(s)} = -0.094n + 0.002Ts_{(s)} + 0.062\mathrm{Is50} + 2.883 \tag{12}$$

$$Vs_{(d)} = -0.093n + 0.063Ts_{(d)} + 0.036\mathrm{Is50} + 2.696 \tag{13}$$

$$Vs_{(s)} = -0.10n + 0.041Ts_{(d)} + 0.004\mathrm{Is50} + 2.892 \tag{14}$$

In Table 4 for all six models, the values of the R^2 are high and RMSE, and the standard error of the estimate (SSE) is low. One of the expectations of MLR is that the errors are independent (errors are the difference between the measured and the values estimated by the MLR models). For checking this assumption, the Durbin-Watson (DW) test is used. The value of DW must be in the range of 1.5 to 2.5 [2, 11]. In the current work, this test shows that the developed relationships can be used (Table 4). Upon conducting an analysis of variance (ANOVA), the levels of significance (*Sig.*) in the models were found to be zero. This outcome suggests that the developed empirical equations are highly suitable for precisely estimating the parameters, as evidenced in Table 4.

The degree of influence of independent variables on the dependent variable is also evaluated by the absolute value of Beta. The higher the value of this coefficient for an independent variable, the greater the effect of that variable

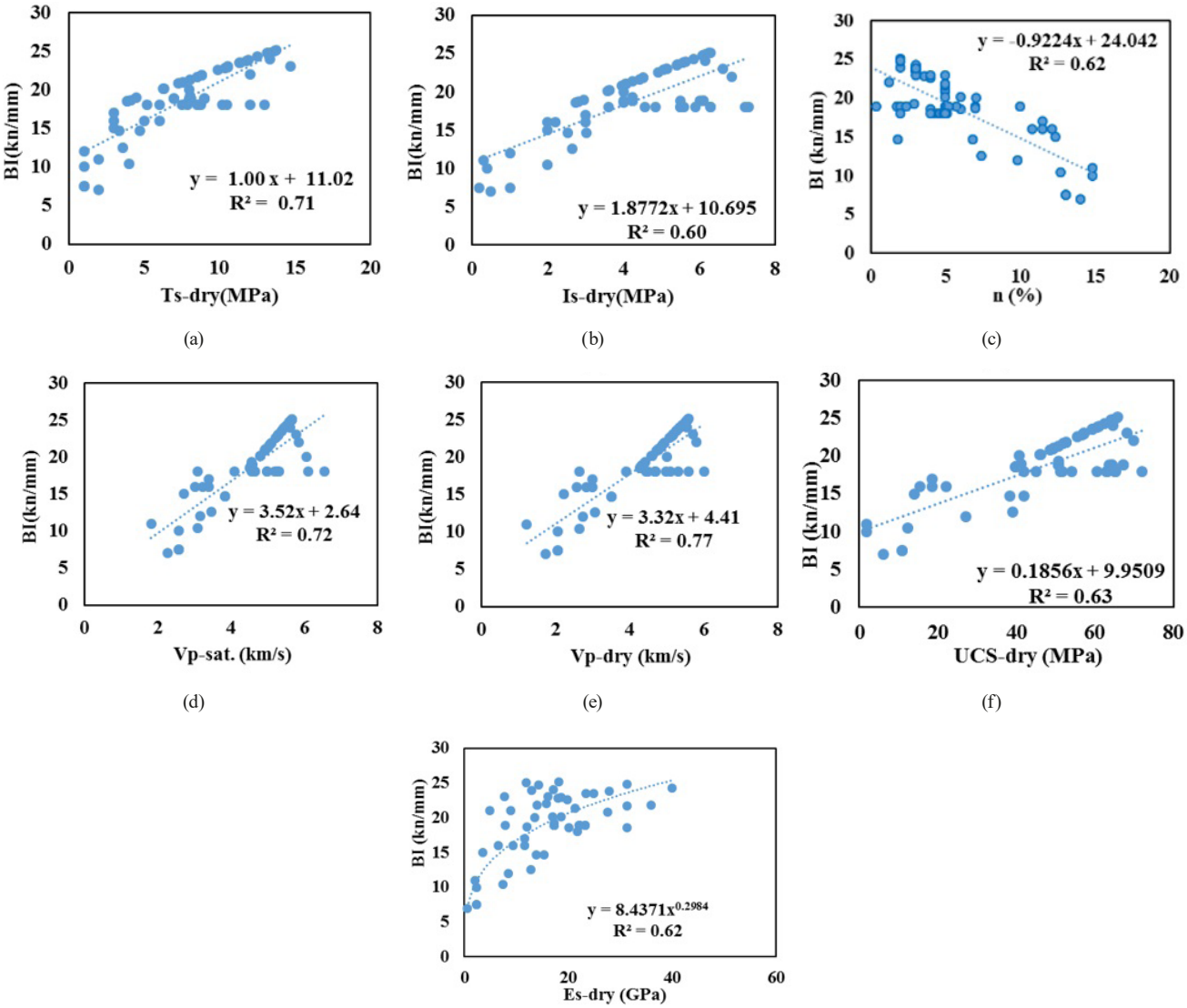

Fig. 3 Relationships of brittleness index with physical and mechanical properties and wave velocities: parts (a) to (g) show the effects of (a) dry tensile strength, (b) dry point load index, (c) porosity, (d) saturated *P*-wave velocity, (e) dry *P*-wave velocity, (f) dry uniaxial compressive strength, and (g) dry static elastic modulus on the brittleness index, respectively

on the *Vs* and BI. In all models, porosity has the greatest impact on the models. In models 9 and 14, the least effect is related to the point load index (Is50) and saturated tensile strength (*Ts-s*), respectively.

4.4 The MFFNN results

To gain the ideal MFFNN, the try-and-error procedure continues until the minimum RMSE is reached [2]. Here, via MATLAB software [43] neurons 1 to 6, based on proposed equations by previous researchers, were evaluated and the results of the most accurate neuron were presented as the optimal neuron. As will be mentioned below, the optimal developed MFFNN models contain 2 neurons in a hidden layer with inputs of porosity (*n*), dry or saturated tensile strength (i.e., *Ts-d* or *Ts-s*) and point load index (Is50) and 3 outputs (such as dry or saturated *Vs* (i.e., *Vs-d* or *Vs-s*), and brittleness index (BI)).

The neuron transfer function at the output layer was selected as Sigmoid and for middle layer was chosen as Purlin. The Levenberg Marquardt training (LMT) algorithm has been applied to teach the models. Also, the Bayesian Regularization (BR) was used to prevent over-fitting at the MFFNN model. In this study, the development of the MFFNN involved randomly allocating the data into three sets: validation, test, and training. The percentages assigned to these sets were 15% for validation, 15% for testing, and 70% for training, selected randomly from the total dataset. The validation set played a crucial

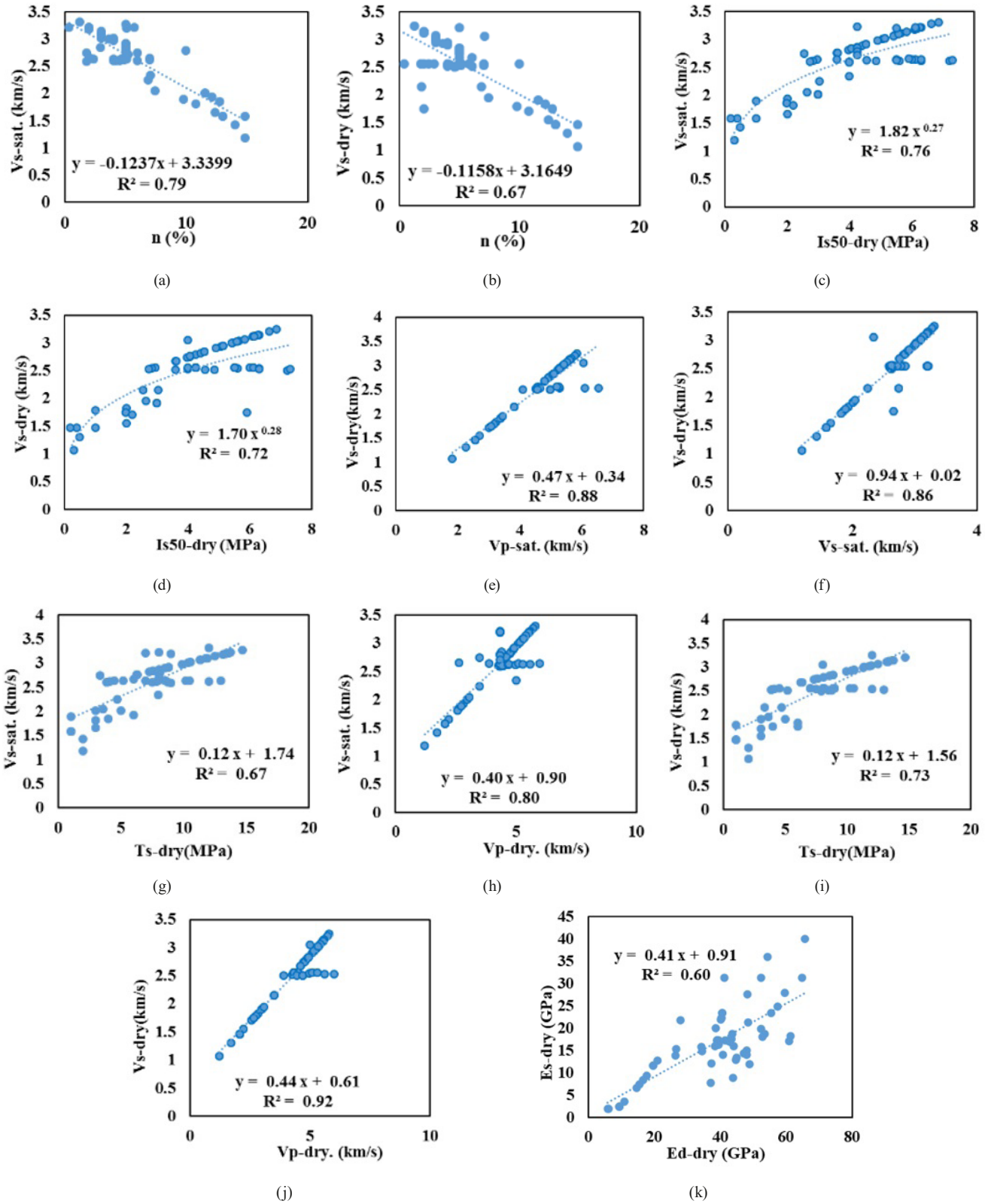

Fig. 4 Effect of variables on *Vs*: the effects of (a) porosity on the saturated shear wave velocity, (b) porosity on the dry shear wave velocity, (c) dry point load index on the saturated shear wave velocity, (d) dry point load index on the dry shear wave velocity, (e) saturated *P*-wave velocity on the dry shear wave velocity, (f) saturated shear wave velocity on the dry shear wave velocity, (g) dry tensile strength on the saturated shear wave velocity, (h) dry *P*-wave velocity on the saturated shear wave velocity, (i) dry tensile strength on the dry shear wave velocity, and (j) dry *P*-wave velocity on the dry shear wave velocity, and (k) dry static elastic modulus on dry dynamic elastic modulus

Table 4 Accuracy of the models

Models	*R*-squared	Adjusted *R*-squared	SSE	RMSE	DW	ANOVA results
BI = *f* (Is50, *Ts-d*, *n*)	0.682	0.67	2.53	3.24	1.88	*F* = 44.40, *Sig.* = 0
BI = *f* (Is50, *Ts-s*, *n*)	0.64	0.62	2.69	4.65	1.78	*F* = 36.87, *Sig.* = 0
Vs-d = *f* (*Ts-s*, *n*, Is50)	0.67	0.65	0.31	2.15	1.62	*F* = 41.50, *Sig.* = 0
Vs-s = *f* (*Ts-s*, *n*, Is50)	0.726	0.71	0.28	2.25	1.88	*F* = 54.90, *Sig.* = 0
Vs-d = *f* (*Ts-d*, *n*, Is50)	0.806	0.80	0.23	2.85	1.80	*F* = 85.99, *Sig.* = 0
Vs-s = *f* (*Ts-d*, *n*, Is50)	0.834	0.83	0.21	3.24	1.63	*F* = 103.5, *Sig.* = 0

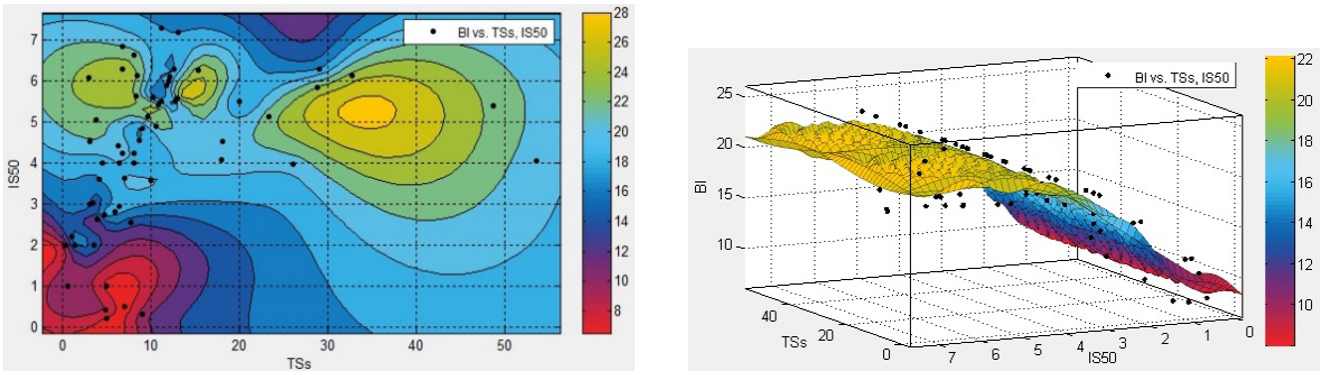

(a) (b)

Fig. 5 Two examples of (a) a contour plot of brittleness index with dry point load index and saturated tensile strength and (b) 3D diagram of brittleness index with dry point load index and saturated tensile strength of the models (Is50 (MPa), *Ts-s* (MPa), BI (kN/mm))

role in preventing overfitting, ensuring that the MFFNN's performance is not overly tailored to the training data. The training set was used to determine the network's weights, enabling it to learn and optimize its performance. The test set was employed to evaluate the MFFNN's results, providing an independent assessment of its performance [2, 11]. The precision of MFFNN models was evaluated using calculating R^2, RMSE, and VAF (Fig. 6). The results for estimating BI and *Vs* in this research showed that the second neuron was the most accurate (an example

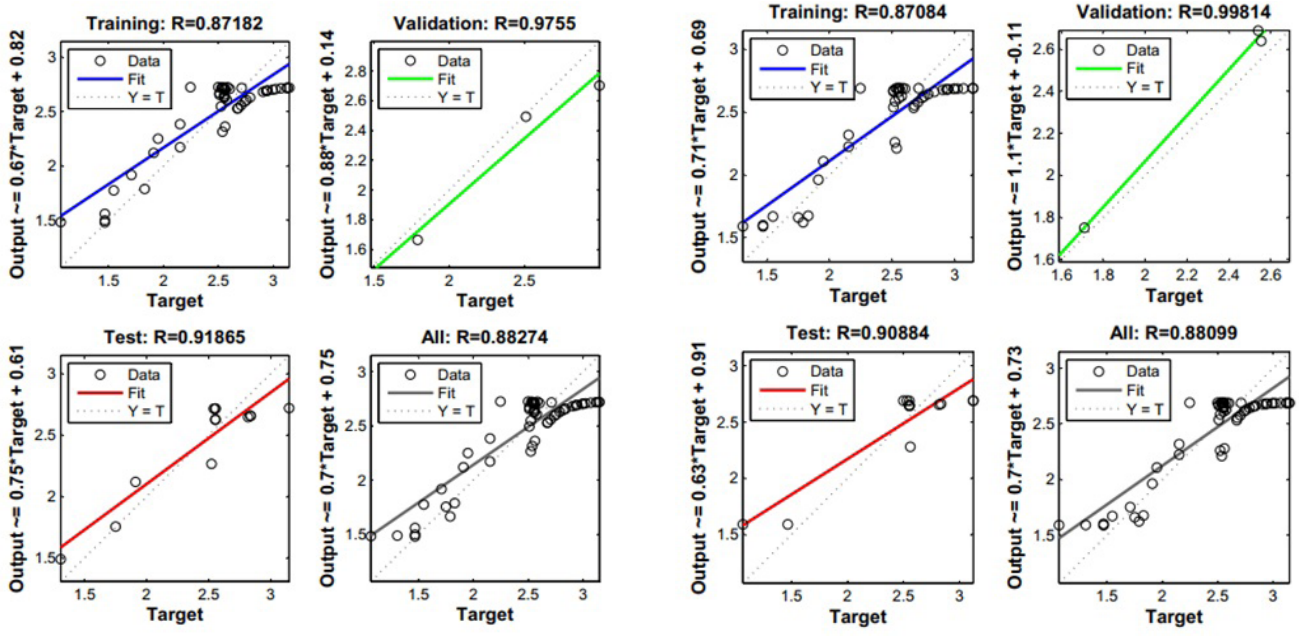

(a) (b)

Fig. 6 An example of correlation coefficients in *Vs-d* prediction by MFFNN ((a) with inputs of *n*, *Ts-s*, IS50) and ((b) with inputs of *n*, IS50, *Ts*-d)

in Fig. 6). Besides the LM algorithms, the performance of other training algorithms such as conjugate gradient and momentum in estimating BI and *Vs* was assessed. Also, the hyperbolic tangent was checked and compared with the sigmoid transfer function. The sigmoid transfer function and the LMT algorithm show the highest efficiency to predict the dependent variables. The results of validation data showed that overfitting did not occur in the models.

Based on MFFNN outcomes, the correlation coefficient of *Vs-d* with independent variables (porosity, dry or saturated tensile strength (*Ts-d* or *Ts-s*) and point load index (Is50)) for the test data are 0.95, and 0.86, respectively. The MLR results also show that the correlation coefficient of *Vs-d* with dry and saturated independent variables are 0.90 and 0.82, respectively. Therefore, in this study the MFFNN is more accurate than MLR for forecasting shear wave velocity and brittleness index. Previous studies have reported similar results [2, 22, 28].

4.5 The GPR results

In this research, 70% of the available data was used for training the GPR models, while the remaining 30% was set aside for testing purposes. The performance of the GPR models was assessed using various criteria, an example presented in Fig. 7. The findings clearly indicate that the GPR method outperformed both the MFFNN and MLR methods in accurately estimating rock brittleness and *Vs*.

4.6 Comparison of methods

The VAF and RMSE values for the GPR, MFFNN, and MLR models are presented in Table 5. Based on Table 5, the effect of independent variables on *Vs* is higher than the brittleness. Also, the effect of independent variables in dry conditions is more than in saturation conditions to increase the accuracy of the brittleness estimation model. On the other hand, the effect of independent variables in saturation conditions is higher than in dry conditions to increase

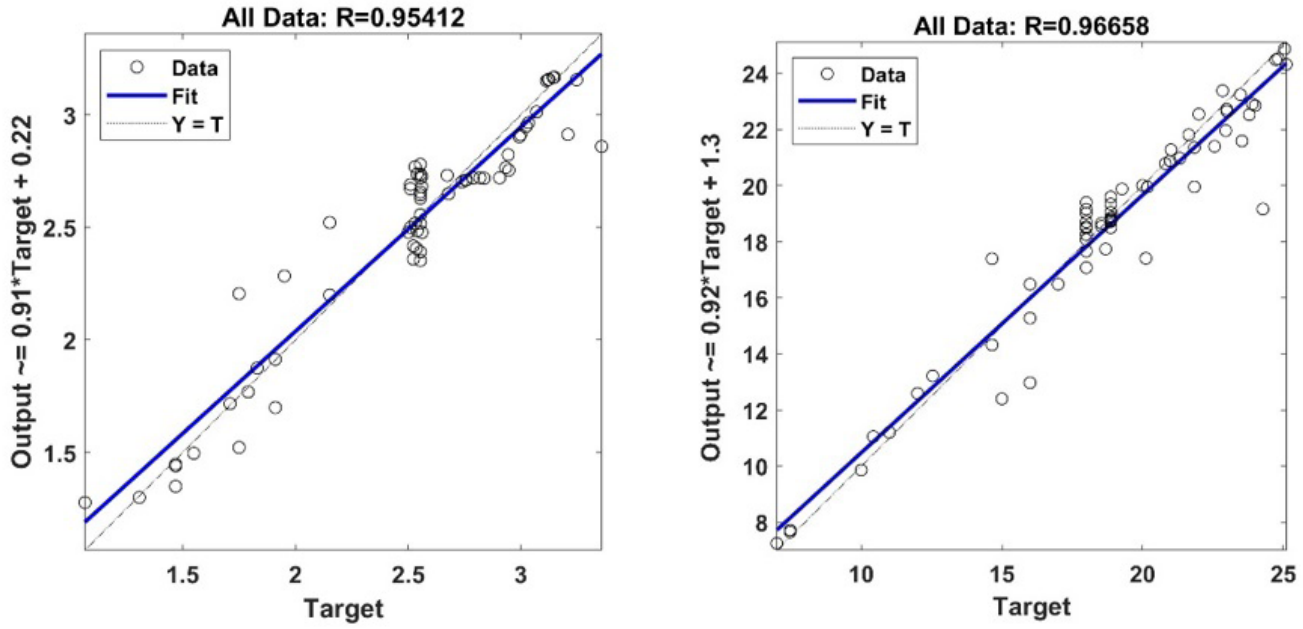

(a) (b)

Fig. 7 An example of correlation coefficients and error histogram of the all data set in BI prediction by GPR: (a) with inputs of *n*, *Ts-s*, Is50; (b) with inputs of *n*, Is50, *Ts-d*

Table 5 Correlation coefficient (*R*), RMSE and %VAF of the test data set for optimum models using MFFNN and GPR methods

Models	MFFNN *R*	GPR *R*	MFFNN RMSE	GPR RMSE	MFFNN %VAF	GPR %VAF
BI = *F* (Is50, *Ts-d*, *n*)	0.94	0.97	1.26	1.38	86.84	88.10
BI = *F* (Is50, *Ts-s*, *n*)	0.92	0.95	2.36	1.122	91.24	84.01
Vs-d = *F* (*Ts-s*, *n*, Is50)	0.87	0.93	4.51	0.25	84.23	85.01
Vs-s = *F* (*Ts-s*, *n*, Is50)	0.87	0.92	4.68	0.155	85.32	81.97
Vs-d = *F* (*Ts-d*, *n*, Is50)	0.94	0.95	1.97	0.14	92.76	89.97
Vs-s = *F* (*Ts-d*, *n*, Is50)	0.96	0.97	1.51	0.18	95.94	96.83

the accuracy of shear wave velocity estimation models. Also, the accuracy of GPR model is higher than MFFNN method (Table 5). Important factors such as the number of inputs, the number of samples, the number of neurons in the hidden layer and hyperparameters (learning rules, activation functions, kernel function type) are effective on the results of intelligent modeling [22, 24]. For example, previous researchers have stated that when the number of samples is small, the support vector machine method works more accurately compared to the MFFNN method due to the use of the structural risk theorem [24].

The estimated *Vs* and BI using GPR, MFFNN and MLR were drawn versus the real *Vs* and BI (Fig. 8). As can be seen, forecasted using MFFNN and GPR approaches are lower than the real values. As a result, the MFFNN and GPR are conservative in estimating *Vs* and BI. While MLR is not conservative in estimating these characteristics.

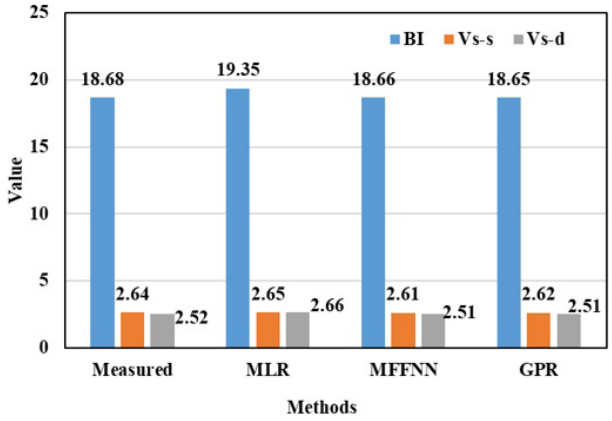

Fig. 8 Comparison of mean of the predicted using used methods with mean of the measured BI and *Vs*

5 Conclusions

In this study, petrographic, brittleness index, and engineering properties of the 66 limestone core specimens of the Asmari formation were assessed in Khersan-II and Bazoft dam sites. Then using SR, GPR, MFFNN, and MLR some empirical relationships were presented to estimate brittleness and *Vs* in saturated and dry situations. The specimens were categorized as Wackestone, Packstone, and Grainstone. Also, the samples with high calcite minerals showed high brittleness and strength properties and low porosity. The MLR results revealed that it is possible to predict brittleness index and *Vs* in both dry and saturated conditions using index tests with high accuracy in the dam sites. Results showed that the GPR performs better than MFFNN and MLR in predicting *Vs*, and brittleness. The effect of moisture on the wave velocity showed that the prediction models for estimating the shear wave velocity in dry conditions (*Vs-d*) were less accurate than the saturated condition (*Vs-s*). Conversely, the relationships presented to estimate the brittleness index in dry conditions are more accurate. Meanwhile, the GPR and MFFNN methods were conservative in estimating these properties. Also, the transfer function of sigmoid and LMT law showed the best performance for forecasting *Vs* and brittleness index.

References

[1] Besharatinezhad, A., Khodabandeh, M. A., Rozgonyi-Boissinot, N., Török, Á. "The Effect of Water Saturation on the Ultrasonic Pulse Velocities of Different Stones", Periodica Polytechnica Civil Engineering, 66(2), pp. 532–540, 2022. https://doi.org/10.3311/PPci.18701

[2] Rastegarnia, A., Lashkaripour, G. R., Sharifi Teshnizi, E., Ghafoori, M. "Evaluation of Engineering Characteristics and Estimation of Static Properties of Clay-Bearing Rocks", Environmental Earth Sciences, 80(18), 621, 2021. https://doi.org/10.1007/s12665-021-09914-x

[3] Abdi, Y., Khanlari, G.-R., Jamshidi, A. "Correlation between Mechanical Properties of Sandstones and P-Wave Velocity in Different Degrees of Saturation", Geotechnical and Geological Engineering, 42(1), pp. 665–674, 2024. https://doi.org/10.1007/s10706-018-0721-6

[4] Karakul, H. "Investigation of Saturation Effect on the Relationship between Compressive Strength and Schmidt Hammer Rebound", Bulletin of Engineering Geology and the Environment, 76(3), pp. 1143–1152, 2017. https://doi.org/10.1007/s10064-016-0883-5

[5] Vasanelli, E., Colangiuli, D., Calia, A., Sileo, M., Aiello, M. A. "Ultrasonic Pulse Velocity for the Evaluation of Physical and Mechanical Properties of a Highly Porous Building Limestone", Ultrasonics, 60, pp. 33–40, 2015. https://doi.org/10.1016/j.ultras.2015.02.010

[6] Ko, T. Y., Kim, T. K., Son, Y., Jeon, S. "Effect of Geomechanical Properties on Cerchar Abrasivity Index (CAI) and its Application to TBM tunelling", Tunnelling and Underground Space Technology, 57, pp. 99–111, 2016. https://doi.org/10.1016/j.tust.2016.02.006

[7] Altindag, R. "Assessment of Some Brittleness Indexes in Rock-Drilling Efficiency", Rock Mechanics and Rock Engineering, 43(3), pp. 361–370, 2010. https://doi.org/10.1007/s00603-009-0057-x

[8] Hucka, V., Das, B. "Brittleness Determination of Rocks by Different Methods", International Journal of Rock Mechanics and Mining Scinces & Geomechanics Abstracts, 11(10), pp. 389–392, 1974. https://doi.org/10.1016/0148-9062(74)91109-7

[9] Ghadernejad, S., Nejati, H. R., Yagiz, S. "A New Rock Brittleness Index on the Basis of Punch Penetration Test Data", Geomechanics and Engineering, 21(4), pp. 391–399, 2020. https://doi.org/10.12989/gae.2020.21.4.391

[10] Yagiz, S., Ghasemi, E., Adoko, A. C. "Prediction of Rock Brittleness Using Genetic Algorithm and Particle Swarm Optimization Techniques", Geotechnical and Geological Engineering, 36(6), pp. 3767–3777, 2018.
https://doi.org/10.1007/s10706-018-0570-3

[11] Shi, X., Liu, G., Cheng, Y., Yang, L., Jiang, H., Chen, L., Jiang, S., Wang, J. "Brittleness Index Prediction in Shale Gas Reservoirs Based on Efficient Network Models", Journal of Natural Gas Science and Engineering, 35, pp. 673–685, 2016.
https://doi.org/10.1016/j.jngse.2016.09.009

[12] Kaunda, R. B., Asbury, B. "Prediction of Rock Brittleness Using Nondestructive Methods for Hard Rock Tunneling", Journal of Rock Mechanics and Geotechnical Engineering, 8(4), pp. 533–540, 2016.
https://doi.org/10.1016/j.jrmge.2016.03.002

[13] Sun, D., Lonbani, M., Askarian, B., Jahed Armaghani, D., Tarinejad, R., Thai Pham, B., Huynh, V. V. "Investigating the Applications of Machine Learning Techniques to Predict the Rock Brittleness Index", Applied Sciences, 10(5), 1691, 2020.
https://doi.org/10.3390/app10051691

[14] Altindag, R., Guney, A. "Predicting the Relationships between Brittleness and Mechanical Properties (UCS, TS and SH) of Rocks", Scientific Research and Essays, 5(16), pp. 2107–2118, 2010. [online] Available at: https://hdl.handle.net/20.500.12809/4536

[15] Akbar, M. N. A., Musu, J. T. "An Extensive Petrophysical Evaluation for Determining Sweet Spot Intervals in the Ultra-Tight Organic-Rich Shale: A Case Study of the North Sumatra Basin", In: SPWLA 2nd Asia Pacific Technical Symposium, Bogor, Java, Indonesia, 2018, SPWLA-2018-1806.

[16] Hadi, F. A., Nygaard, R. "Shear Wave Prediction in Carbonate Reservoirs: Can Artificial Neural Network Outperform Regression Analysis?", In: 52nd U.S. Rock Mechanics/Geomechanics Symposium, Seattle, WA, USA, 2018, ARMA-2018-905.

[17] Wang, P., Peng, S. "On a New Method of Estimating Shear Wave Velocity from Conventional Well Logs", Journal of Petroleum Science and Engineering, 180, pp. 105–123, 2019.
https://doi.org/10.1016/j.petrol.2019.05.033

[18] Singh, S., Kanli, A. I. "Estimating Shear Wave Velocities in Oil Fields: A Neural Network Approach", Geosciences Journal, 20(2), pp. 221–228, 2016.
https://doi.org/10.1007/s12303-015-0036-z

[19] Alizadeh, S. M., Iraji, A., Tabasi, S., Ahmed, A. A. A., Motahari, M. R. "Estimation of Dynamic Properties of Sandstones Based on Index Properties Using Artificial Neural Network and Multivariate Linear Regression Methods", Acta Geophysica, pp. 225–242, 2022.
https://doi.org/10.1007/s11600-021-00705-3

[20] Mehrad, M., Ramezanzadeh, A., Bajolvand, M., Reza Hajsaeedi, M. "Estimating Shear Wave Velocity in Carbonate Reservoirs from Petrophysical Logs Using Intelligent Algorithms", Journal of Petroleum Science and Engineering, 212, 110254, 2022.
https://doi.org/10.1016/j.petrol.2022.110254

[21] Al-Dousari, M., Garrouch, A. A., Al-Omair, O. "Investigating the Dependence of Shear Wave Velocity on Petrophysical Parameters", Journal of Petroleum Science and Engineering, 146, pp. 286–296, 2016.
https://doi.org/10.1016/j.petrol.2016.04.036

[22] Zheng, J., Shen, M., Motahari, M. R., Khajehzadeh, M. "Prediction of Rock Tensile Strength Using Soft Computing and Statistical Methods", Periodica Polytechnica Civil Engineering, 67(3), pp. 902–913, 2023.
https://doi.org/10.3311/PPci.22179

[23] Gao, W., Karbasi, M., Hasanipanah, M., Zhang, X., Guo, J. "Developing GPR Model for Forecasting the Rock Fragmentation in Surface Mines", Engineering with Computers, 34(2), pp. 339–345, 2018.
https://doi.org/10.1007/s00366-017-0544-8

[24] Fang, Z., Cheng, J., Xu, C., Xu, X., Qajar, J., Rastegarnia, A. "Comparison of machine learning and statistical approaches to estimate rock tensile strength", Case Studies in Construction Materials, e02890, 2024.
https://doi.org/10.1016/j.cscm.2024.e02890

[25] Jahed Armaghani, D., Asteris, P. G., Askarian, B., Hasanipanah, M., Tarinejad, R., Huynh, V. V. "Examining Hybrid and Single SVM Models with Different Kernels to Predict Rock Brittleness", Sustainability, 12(6), 2229, 2020.
https://doi.org/10.3390/su12062229

[26] Viswanathan, R., Samui, P. "Determination of Rock Depth Using Artificial Intelligence Techniques", Geoscience Frontiers, 7(1), pp. 61–66, 2016.
https://doi.org/10.1016/j.gsf.2015.04.002

[27] Mahmoodzadeh, A., Mohammadi, M., Farid Hama Ali, H., Nariman Abdulhamid, S., Hashim Ibrahim, H., M Gharrib Noori, K. "Dynamic Prediction Models of Rock Quality Designation in Tunneling Projects", Transportation Geotechnics, 27, 100497, 2021.
https://doi.org/10.1016/j.trgeo.2020.100497

[28] Lawal, A. I., Kwon, S., Aladejare, A. E., Oniyide, G. O. "Prediction of the Static and Dynamic Mechanical Properties of Sedimentary Rock Using Soft Computing Methods", Geomechanics and Engineering, 28(3), pp. 313–324, 2022.
https://doi.org/10.12989/gae.2022.28.3.313

[29] Lee, J., Lumley, D. E. "Predicting Shale Mineralogical Brittleness Index from Seismic and Elastic Property Logs Using Interpretable Deep Learning", Journal of Petroleum Science and Engineering, 220, 111231, 2023.
https://doi.org/10.1016/j.petrol.2022.111231

[30] Li, D., Han, M., Zhu, Q. "Evaluation of Rock Brittleness Index under Dynamic Load", Applied Sciences, 13(8), 4698, 2023.
https://doi.org/10.3390/app13084698

[31] Fang, X., Feng, H., Zhang, Z., Li, F. "Brittleness Index Prediction Method of Tight Reservoir Based on Grey Correlation and Analytic Hierarchical Process", Petroleum Science and Technology, 2023.
https://doi.org/10.1080/10916466.2023.2172431

[32] Brown, E. T. "Rock Characterization Testing and Monitoring: ISRM Suggested Methods", Pergamon Press, 1981. ISBN 9780080273099

[33] ASTM "ASTM D2845-08 Standard Test Method for Laboratory Determination of Pulse Velocities and Ultrasonic Elastic Constants of Rock", ASTM International, West Conshohocken, PA, USA, 2008.

[34] ASTM "ASTM D3967-95(a)(2001) Standard Test Method for Splitting Tensile Strength of Intact Rock Core Specimens", ASTM International, West Conshohocken, PA, USA, 2001.
https://doi.org/10.1520/D3967-95AR01

[35] ASTM "ASTM D5731-02 Standard Test Method for Determination of the Point Load Strength Index of Rock", ASTM International, West Conshohocken, PA, USA, 2002.
https://doi.org/10.1520/D5731-02

[36] Yagiz, S. "Assessment of Brittleness Using Rock Strength and Density with Punch Penetration Test", Tunnelling and Underground Space Technology, 24(1), pp. 66–74, 2009.
https://doi.org/10.1016/j.tust.2008.04.002

[37] Dunham, R. J. "Classification of Carbonate Rocks According to Depositional Textures", In: Ham, W. E. (ed.) M1: Classification of Carbonate Rocks--A Symposium, The American Association of Petroleum Geologists, Tulsa, OK, USA, 1962, pp. 108–121.

[38] AFTES "Guidelines for Characterization of Rock Masses Useful for the Design and the Construction of Underground Structures", French Tunnelling and Underground Space Technology, Paris, France, Rep. 177, 2003.

[39] Atzeni, C., Sanna, U., Spanu, N. "Some Mechanisms of Microstructure Weakening in High-Porous Calcareous Stones", Materials and Structures, 39(5), pp. 525–531, 2006.
https://doi.org/10.1007/s11527-005-9044-1

[40] Török, Á., Vásárhelyi, B. "The Influence of Fabric and Water Content on Selected Rock Mechanical Parameters of Travertine, Examples from Hungary", Engineering Geology, 115(3–4), pp. 237–245, 2010.
https://doi.org/10.1016/j.enggeo.2010.01.005

[41] Vásárhelyi, B. "Statistical Analysis of the Influence of Water Content on the Strength of the Miocene Limestone", Rock Mechanics and Rock Engineering, 38(1), pp. 69–76, 2005.
https://doi.org/10.1007/s00603-004-0034-3

[42] Taylor, R. "Interpretation of the Correlation Coefficient: A Basic Review", Journal of Diagnostic Medical Sonography, 6(1), pp. 35–39, 1990.
https://doi.org/10.1177/875647939000600106

[43] MathWorks "MATLAB, (2014a)", [computer program] The MathWorks, Inc., Natick, MA, USA, 2014.